bioRxiv preprint doi: https://doi.org/10.1101/2021.02.20.432088; this version posted February 20, 2021. The copyright holder for this preprint (which was not certified by peer review) is the author/funder, who has granted bioRxiv a license to display the preprint in perpetuity. It is made available under aCC-BY-NC-ND 4.0 International license.

Improving stroke detection via Correlation Tensor MRI

Rita Alves[1], Rafael Neto Henriques[1], Leevi Kerkelä[2], Cristina Chavarrías[1], Sune N Jespersen[3,4], Noam Shemesh[1†]

[1]Champalimaud Research, Champalimaud Centre for the Unknown, Lisbon Portugal
[2]*UCL Great Ormond Street Institute of Child Health, University College London, London, United Kingdom*
[3]Center of Functionally Integrative Neuroscience (CFIN) and MINDLab, Clinical Institute, Aarhus University, Aarhus, Denmark
[4]Department of Physics and Astronomy, Aarhus University, Aarhus, Denmark

[†]Corresponding author:
Dr. Noam Shemesh, Champalimaud Research, Champalimaud Centre for the Unknown
Av. Brasilia 1400-038, Lisbon, Portugal.
E-mail: noam.shemesh@neuro.fchampalimaud.org;
Phone number: +351 210 480 000 ext. #4467.

bioRxiv preprint doi: https://doi.org/10.1101/2021.02.20.432088; this version posted February 20, 2021. The copyright holder for this preprint (which was not certified by peer review) is the author/funder, who has granted bioRxiv a license to display the preprint in perpetuity. It is made available under aCC-BY-NC-ND 4.0 International license.

ABSTRACT

Noninvasively detecting and characterizing modulations in cellular scale micro-architecture is a desideratum for contemporary neuroimaging. Diffusion MRI (dMRI) has become the mainstay methodology for probing microstructure, and, in ischemia, its contrasts have revolutionized stroke management. However, the sources of the contrasts observed in conventional dMRI in general and in ischemia in particular are still highly debated since the markers are only surrogate reporters of the underlying microstructure. Here, we present Correlation Tensor MRI (CTI), a method that rather than measuring diffusion, harnesses diffusion correlations as its source of contrast. We show that CTI can resolve the sources of diffusional kurtosis, which in turn, provide dramatically enhanced specificity and sensitivity towards ischemia. In particular, the sensitivity towards ischemia nearly doubles, both in grey matter and white matter, and unique signatures for neurite beading, cell swelling, and edema are inferred from CTI. The enhanced sensitivity and specificity endowed by CTI bodes well for future applications in biomedicine, basic neuroscience, and in the clinic.

bioRxiv preprint doi: https://doi.org/10.1101/2021.02.20.432088; this version posted February 20, 2021. The copyright holder for this preprint (which was not certified by peer review) is the author/funder, who has granted bioRxiv a license to display the preprint in perpetuity. It is made available under aCC-BY-NC-ND 4.0 International license.

INTRODUCTION

Longitudinal modulations in tissue micro-architecture are associated with diverse natural neural processes including development[1], plasticity[2], memory[3], learning[4,5], connectivity between brain areas[6,7], ageing[8], and recovery from injury[9]. Adverse micro-architectural alterations in the neural tissue milieu are also associated with psychiatric disorders such as depression[10], neurodegenerative diseases such as Parkinson's disease[11] and Alzheimer's disease[12], and injuries such as ischemic stroke[9] and traumatic brain injury[13]. In ischemic stroke – one of the leading causes of disability and death worldwide[14] – a complex cascade of micro-architectural events occurs acutely following a blood vessel occlusion and the ensuing metabolic and aerobic deprivation[15]. These micro-architectural modifications include neurite beading[16], intracellular swelling due to loss of ion homeostasis, cytotoxic edema, and cell death (Fig. 1a) followed later by disruptions in the blood-brain barrier, vasogenic edema and tissue clearance at later stages. The extent of these processes later determines the prognosis, the potential for functional recovery[17] and success of treatment.

Given the longitudinal nature of micro-architectural modulations in neural tissue, non-invasive mapping of tissue microstructure[18,19] plays a pivotal role in assessing enhancements in microstructure (e.g., due to learning) as well as adverse effects upon disease or neural injury. Diffusion-weighted magnetic resonance imaging (DWI) – a non-invasive methodology capable of imparting contrast sensitive to motion of water molecules in the tissue[20], thereby indirectly probing their interaction with the microscopic boundaries imposed by the cellular environment[21] – has completely revolutionized our ability to follow microstructural modulations over extended periods of time. In stroke, the quantification of apparent diffusion coefficients (ADCs) provided the first effective means of early stroke detection[22,23], thereby facilitating the administration of treatment within the limited time window of operation[24]. Diffusion Tensor MRI (DTI[25]), quantifying the entire diffusion tensor rather than only a single ADC, provided detailed information on anisotropy and orientation of white matter tracts. Diffusion Kurtosis MRI (DKI)[26],

bioRxiv preprint doi: https://doi.org/10.1101/2021.02.20.432088; this version posted February 20, 2021. The copyright holder for this preprint (which was not certified by peer review) is the author/funder, who has granted bioRxiv a license to display the preprint in perpetuity. It is made available under aCC-BY-NC-ND 4.0 International license.

quantifying a fourth order diffusional kurtosis tensor, enabled a more refined analysis of anisotropy and magnitude of non-gaussian diffusion effects in neural tissues.

Still, the main limitation of all such dMRI measurements is that they rely on the concept of "Single Diffusion Encoding" (SDE[27,28]): a single epoch in which diffusion contrast is imparted. In such a scenario, all potential sources for microstructural modulations are conflated due to the inherent averaging of diffusion propagators within the imaged voxel. In other words, SDE signal does not carry sufficient information for distinguishing the sources underlying different microstructural effects and the metrics extracted are surrogate markers of micro-architecture. In stroke, for example, effects arising from cross-sectional variations due to neurite beading[16,29] (Fig.1a, purple) from cell body swelling (Fig.1a, light blue) or the transcapillary ionic edema (Fig1.a dark blue), are notoriously difficult to decipher. Notably, the biophysical underpinnings of even the simplest ADC changes observed in stroke[30,31] have been vigorously debated for the last three decades[16,32,33]. The parameters estimated from such SDE approaches, including mean diffusivity (MD), fractional anisotropy (FA), or total kurtosis[34] (K_T) thus suffer from lack of specificity.

Here, we depart from the convention of mapping displacement-driven tensors (D, K), and rather harness Double Diffusion Encoding – a method applying two diffusion-sensitizing epochs that probe the correlation between diffusion modes in different directions[28,35,36] – for quantitatively mapping the properties of a 4th order displacement correlation tensor[37]. Such Correlation Tensor MRI (CTI[38]) measurements then offer the possibility of disentangling the different underlying sources of non-gaussian diffusion: anisotropic kurtosis[39], K_{aniso}; isotropic kurtosis[40], K_{iso}; and microscopic kurtosis[41], μK (Fig.1c). In particular, K_{aniso} quantifies the degree of anisotropy in the tissue irrespective of orientation dispersion effects; K_{iso} quantifies the variance in diffusivities within the tissue; and μK quantifies the degree of structural disorder[29] and restricted diffusion[42]. Each of these sources represent fundamentally different contributions to diffusion and therefore their measurement can greatly enhance specificity. We present the first CTI experiments in a stroke model, which evidence unique signatures for the different underlying micro-architectural modulations, including beading, swelling and edema.

bioRxiv preprint doi: https://doi.org/10.1101/2021.02.20.432088; this version posted February 20, 2021. The copyright holder for this preprint (which was not certified by peer review) is the author/funder, who has granted bioRxiv a license to display the preprint in perpetuity. It is made available under aCC-BY-NC-ND 4.0 International license.

Importantly, the sensitivity towards stroke detection is dramatically increased by this approach.

CTI thus endows the sought-after specificity and sensitivity towards microstructural features.

Implications for microstructural imaging and future applications are discussed.

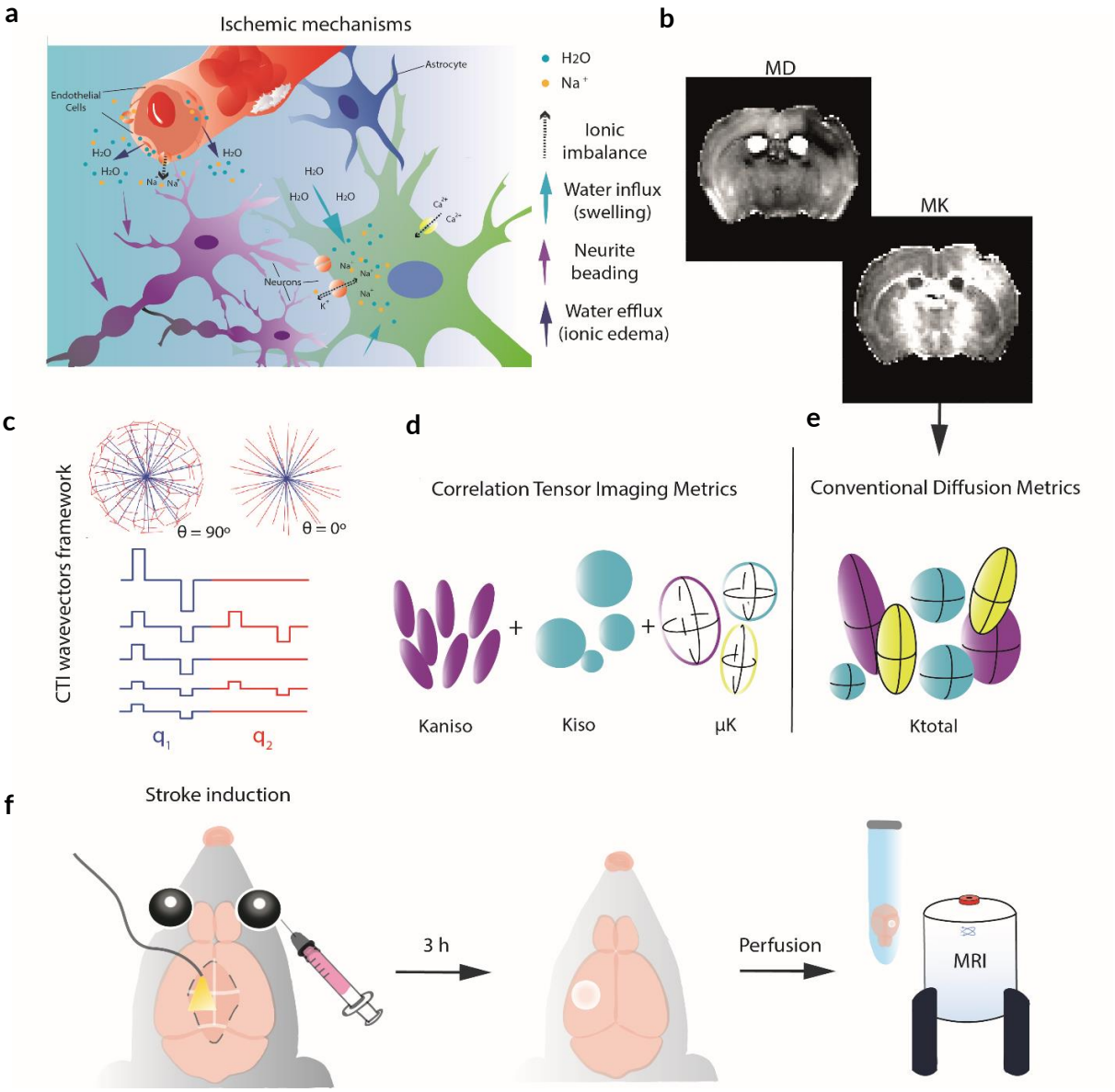

Figure 1: Acute ischemic mechanisms, CTI elements illustration and stroke experimental set up. (a) At an acute ischemic phase – after vascular occlusion – microscopic disturbances such as ionic imbalance (dashed), cell swelling (light blue arrows account for an excessive cellular influx of water in endothelial and neuronal cells), with a subsequent neurite beading (purple) are occurring (cytotoxic edema). This event is followed by ionic edema – transcapillary flux of Na+ and water efflux (dark blue arrows). The blood brain barrier remains intact at this stage. (b) Mean diffusivity (MD) and total kurtosis (MK) are presented as (e) conventional diffusion metrics. Although conventional diffusion metrics obtained from single diffusion encoding (SDE) techniques assess quantitative information on tissue heterogeneity, these cannot resolve the different kurtosis sources, hence lacking specificity and hampering an accurate association with biophysical alterations. On the other hand, correlation tensor imaging (CTI), relying on the cumulant expansion of Double Diffusion Encoding (DDE) signal with (c) 90º and 0º combinations of wavevectors, enables the disentanglement of the kurtosis sources (d) (Anisotropic Kurtosis, Kaniso; Isotropic Kurtosis, Kiso; and Microscopic Kurtosis, μK), providing a more specific characterization of the microscopic alterations occurring in ischemic tissue. (f) A photothrombotic model was used in order to induce a well delimited focal infarct. Upon longitudinal incision and target region coordinates identification (S1bf), irradiation on the left hemisphere was performed for 15 minutes. At 3 h post irradiation offset, the brains were extracted via transcardial perfusion and placed in an NMR tube with Fluorinert for MRI imaging.

bioRxiv preprint doi: https://doi.org/10.1101/2021.02.20.432088; this version posted February 20, 2021. The copyright holder for this preprint (which was not certified by peer review) is the author/funder, who has granted bioRxiv a license to display the preprint in perpetuity. It is made available under aCC-BY-NC-ND 4.0 International license.

RESULTS

Focal thrombi induction.

Upon injection with photosensitive dye and irradiation with the appropriate wavelength (Fig.1f) for generation of reactive oxygen species that in turn produce severe endothelial damage and thrombi formation, a well-delineated extensive stroke was evidenced in T_2-weighted images (Fig. 2b) 3h post-ischemia. The affected area appeared with strong hyperintense contrast, unilaterally covering the barrel cortex and to some extent the hippocampus. The powder-averaged diffusion-weighted contrasts (Fig.2b) also clearly delineated the stroke area as hyperintense signals. For all five mice that underwent the ischemia induction, the stroke area was highly reproducible (Fig. S1). By contrast, no interhemispheric differences could be observed in the control mice that were injected with the photosensitive dye but did not undergo irradiation (Fig.2c-d). Both T2-weighted images and powder-averaged diffusion-weighted images appear symmetric and without abnormal contrasts.

A histological evaluation of the stroked area (Fig.2e) clearly demonstrated abnormalities in Nissl Cresyl violet staining. The zoomed in view of the ipsilesional cortex (Fig.2e, right) also shows the reduced staining and density, compared with the contralesional cortex (Fig.2e, left).

bioRxiv preprint doi: https://doi.org/10.1101/2021.02.20.432088; this version posted February 20, 2021. The copyright holder for this preprint (which was not certified by peer review) is the author/funder, who has granted bioRxiv a license to display the preprint in perpetuity. It is made available under aCC-BY-NC-ND 4.0 International license.

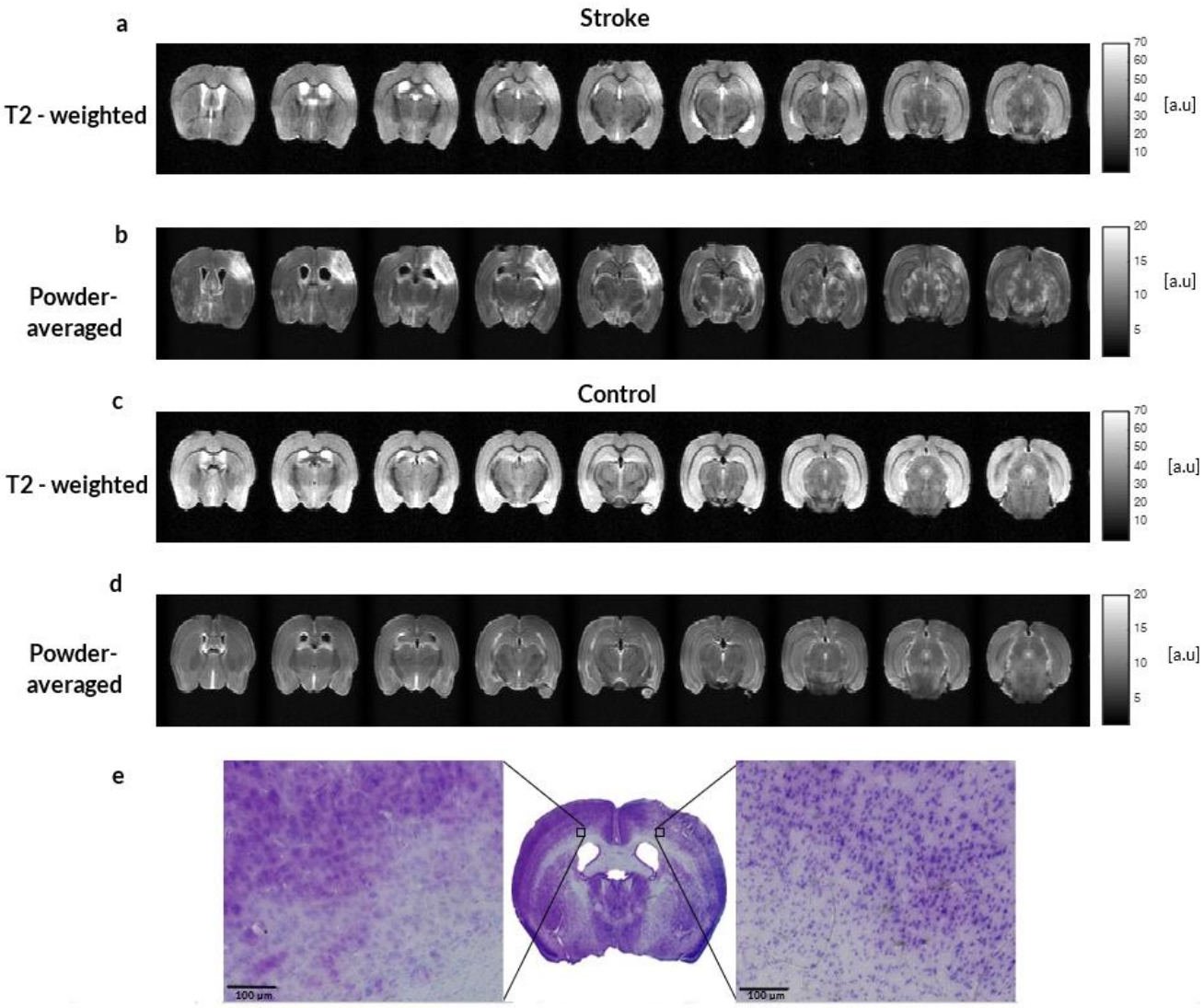

Figure 2: Raw T2-weighted, powder-averaged data and histological validation of the lesion. (a, c) T2-weighted images and total excess kurtosis of (b, d) the powder-averaged signal decays over 135 directions of diffusion wave vectors from representative extracted brains from the stroke and control groups (total b-value = 3000 s/mm^2). 9 representative coronal slices are presented from rostral to caudal direction. The T2-weighted contrast shows elevated intensity values towards the infarcted region (left hemisphere) gray matter, whereas the powder-averaged contrast presents elevated values for both gray and white matter within the infarcted region. (e) Histological analysis was performed to assess cell damage and validate the lesion. A Nissl Cresyl violet stained brain section is presented, showing the lesion in the subcortical region of the left hemisphere from a representative mouse brain perfused at 3 hours post ischemic stroke. A critical selected GM region in the ipsilesional hemisphere was magnified (53x), presenting cell damage associated with necrosis and a brighter coloured and less packed region in the lesion site associated with cell loss, when compared to the intact contralesional region (left).

bioRxiv preprint doi: https://doi.org/10.1101/2021.02.20.432088; this version posted February 20, 2021. The copyright holder for this preprint (which was not certified by peer review) is the author/funder, who has granted bioRxiv a license to display the preprint in perpetuity. It is made available under aCC-BY-NC-ND 4.0 International license.

Conventional contrast in stroke

Total kurtosis and MD. As in prior studies[43,44], we observed strongly elevated total kurtosis values in the stroked group. Fig.3a shows the clearly elevated values of K_T in a representative mouse brain in the affected hemisphere, as well as reduced mean diffusivity and slightly reduced fractional anisotropy (Fig.S2). The K_t values appeared elevated both in gray matter and white matter, and the contrast was more apparent compared with the MD contrast. On the other hand, no interhemispheric differences were observed in total kurtosis in the control group (c.f. Fig.3b for a representative control brain) and other diffusion tensor metrics (MD, FA were also symmetric (Fig.S2). However, it is difficult to draw conclusions on the sources for stroke-induced the changes in K_t, which could involve any of the mechanisms described in Fig.1a, as also represented in the illustration of kurtosis sources (Fig.3c).

CTI contrast in stroke

Given that CTI can further disentangle the different sources, we next turn to evaluate the differences observed in CTI's metrics.

Microscopic Kurtosis (µK). The µK metric derived from the CTI analysis in the stroked brains was dramatically elevated in the affected area (Fig.3d). This observation was consistent for all N = 5 mice (Fig. S3), and a visual examination shows that the elevated µK appeared higher both in gray matter and white matter tissues. It is further noteworthy that the stroke was much better delineated in the µK maps compared with the conventional total kurtosis counterparts (c.f. below for quantitative analyses). In the control group, again the µK maps showed no striking interhemispheric differences (Fig.3e), suggesting that these measurements representing structural disorder (Fig.3f) do not arise from some unknown asymmetric left-right imaging artifact.

Isotropic variance (K_{iso}). The isotropic variance contrast derived from CTI analysis exhibited increases, mainly evident in white matter, and much less noticeable contrast differences in gray matter (Fig.3g). No apparent differences in white or gray matter tissues were observed between hemispheres for K_{iso} in the control group (Fig.3h), suggesting that the

bioRxiv preprint doi: https://doi.org/10.1101/2021.02.20.432088; this version posted February 20, 2021. The copyright holder for this preprint (which was not certified by peer review) is the author/funder, who has granted bioRxiv a license to display the preprint in perpetuity. It is made available under aCC-BY-NC-ND 4.0 International license.

variance in isotropic tensor magnitudes (Fig.3i) in the stroked group is again not related with some imaging source.

Anisotropic variance (K_{aniso}). The anisotropic variance contrast in stroke evidenced strong reductions in K_{aniso}, more evident in the ipsilesional gray matter (Fig.3j) but also showing some reductions in white matter. In the control group, the same K_{aniso} contrast did not appear different between the hemispheres (Fig.3k). In other words, the gray matter in the stroked hemisphere was characterized by decreased local anisotropy, independent of local orientation (Fig.3l).

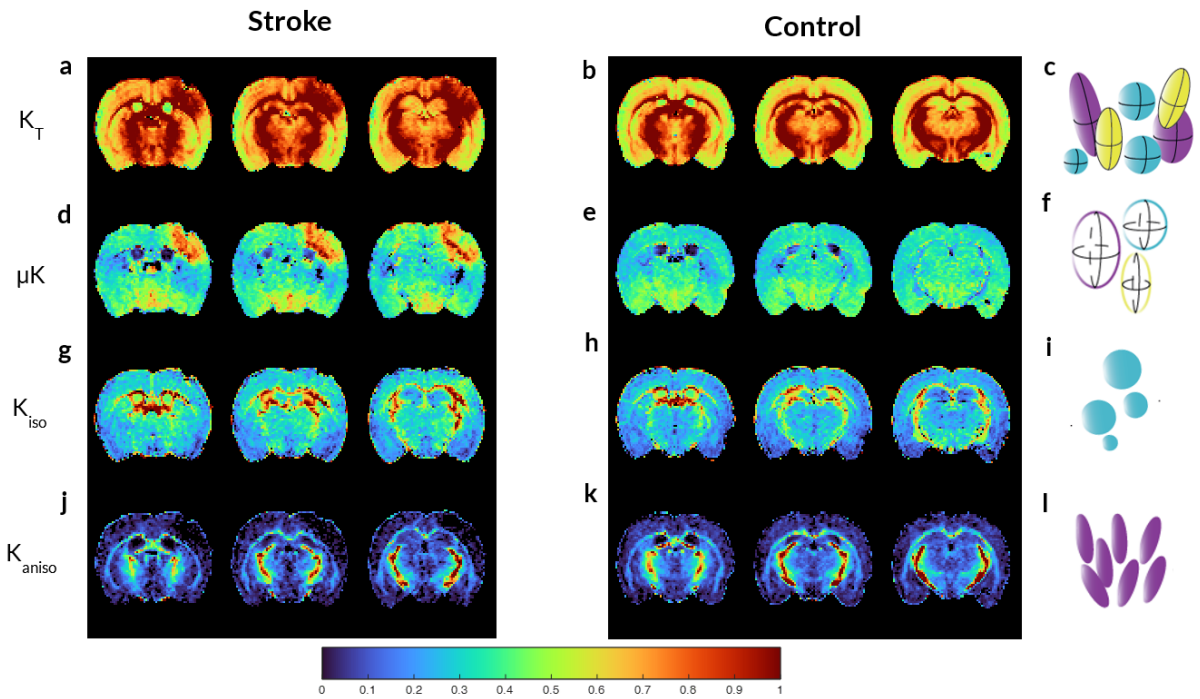

Figure 3: Kurtosis sources maps for stroked and control brains. Kurtosis maps ((a, b) K_T, (d, e) μK, (g, h) K_{iso} and (j, k) K_{aniso}) for three slices from representative brains from the stroke (left) and control (right) groups are presented with respective illustration of each kurtosis source (c, f, i, l). In the stroke group, the ipsilesional hemisphere shows higher K_T intensity values in gray matter and a clear distinction between hemispheres is observed in μK values, showing greater intensities in both white and gray matter. K_{aniso} presents lower values in both white and gray matter within the ipsilesional hemisphere when compared to the contralesional hemisphere (scale 0-1 [a.u]).

To examine whether the stroked area could be better delineated using CTI metrics we plotted a 3D render of the μK maps and compared them to their conventional total kurtosis counterpart in a representative brain (Fig.4). The entire 3D render can be viewed in

bioRxiv preprint doi: https://doi.org/10.1101/2021.02.20.432088; this version posted February 20, 2021. The copyright holder for this preprint (which was not certified by peer review) is the author/funder, who has granted bioRxiv a license to display the preprint in perpetuity. It is made available under aCC-BY-NC-ND 4.0 International license.

Supplementary Videos, and the slice-by-slice data can be viewed for every animal in Figures S4-S5). These depictions of the stroke reveal how µK provides a much more sensitive delineation of the affected area. Both the area affected, and the magnitude of the effect are much more readily read from the µK 3D render.

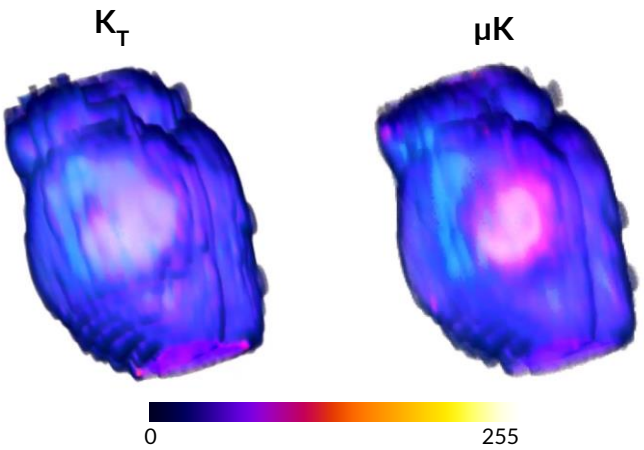

Figure 4: 3D rendering maps for K_T and µK. Volume render maps using tricubic smooth interpolation for K_T and µK sources in a representative stroke group brain. µK shows a more elevated contrast in the ipsilesional hemisphere (delineating the affected region by the lesion) in comparison to K_T (RGB).

Quantitative sensitivity analyses of different kurtosis sources in stroke

To assess whether the CTI metrics provide a more sensitive evaluation of stroke, we analysed the percent changes for all affected voxels (gray matter and white matter combined (Fig.S7)) as well as for gray matter and white matter separately. Fig.5a shows the magnitude of the effects (both with respect to the contralesional hemisphere in the stroked group as well as the ipsilateral hemisphere in control mice). While total kurtosis changes ~40% of its nominal value in stroke, the µK contrast in GM+WM was nearly double, with ~80% change of its nominal values. While K_t changes were quite similar between GM and WM, the µK changed more dramatically in WM (~100%) and still very strongly in GM (~75%). K_{iso} on the other hand, changed only by ~40% in general, with higher affinity to WM (~70% change but with large standard error). Finally, K_{aniso} decreased by over 50% overall, with nearly -90% changes in GM and -30% changes in WM.

bioRxiv preprint doi: https://doi.org/10.1101/2021.02.20.432088; this version posted February 20, 2021. The copyright holder for this preprint (which was not certified by peer review) is the author/funder, who has granted bioRxiv a license to display the preprint in perpetuity. It is made available under aCC-BY-NC-ND 4.0 International license.

We then asked whether CTI metrics show a higher count of involved voxels compared with the conventional K_t. The analysis (Fig.5b) clearly demonstrates that μK is able to detect more affected voxels (~17% more) overall, with a higher affinity towards GM, while K_t is more sensitive in WM. K_{iso} and K_{aniso} do not detect more affected voxels than K_t (Fig.5b).

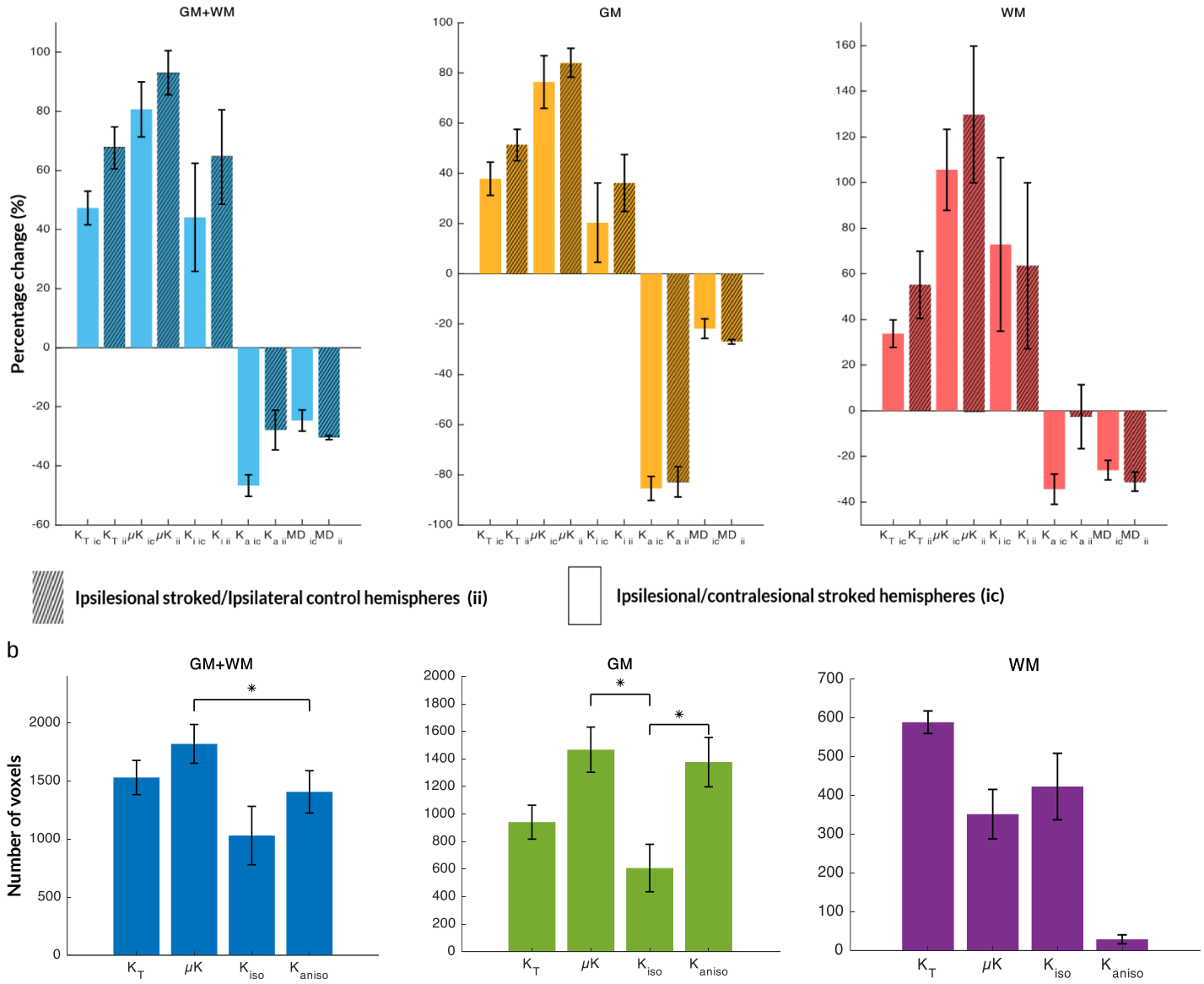

Figure 1: (a) Mean ipsilesional-contralesional ratio (unstriped pattern bars [ic]) accounting for the mean values of all voxels for different ROIs – gray matter (GM) and white matter (WM) – from five stroked brains (N = 5) and mean ipsilesional-ipsilateral control ratio (striped pattern bars [ii]) accounting for the mean of all voxels for different ROIs from five stroked and five control group hemispheres (mean ± standard error of the mean) were assessed for K_T, μK, K_{iso}, K_{aniso} and Mean Diffusivity (MD). Percentage change was distinctly more elevated for both GM and WM in μK. No statistically significant differences were reported ($p < 0.05$); (b) A quantitative analysis was performed based on the number of voxels which present abnormal contrast in the ipsilesional hemisphere when compared to the contralesional hemisphere. Significant differences were reported between μK and K_{aniso} in total lesion (GM + WM); between μK and K_{iso} in GM; between K_{iso} and K_{aniso} in GM ($p < 0.05$). μK presented in our study more abnormal voxels accounting for total lesion and GM, whereas K_T presented more abnormal voxels in WM.

bioRxiv preprint doi: https://doi.org/10.1101/2021.02.20.432088; this version posted February 20, 2021. The copyright holder for this preprint (which was not certified by peer review) is the author/funder, who has granted bioRxiv a license to display the preprint in perpetuity. It is made available under aCC-BY-NC-ND 4.0 International license.

In-vivo CTI in stroke

To ensure that the effects above were not dominated by fixation effects upon perfusion of the brains, and to show the in vivo feasibility of the approach we repeated the same experiments at the 3h time point post-ischemia in an in vivo setting. Fig. S8 shows that the same trends as observed in the ex vivo results reported above persist; most importantly, the dramatic elevation of μK persists in all tissues, K_{iso} is increased in WM, and K_{aniso} decreases in GM. Therefore, all the trends above are reproduced in vivo.

bioRxiv preprint doi: https://doi.org/10.1101/2021.02.20.432088; this version posted February 20, 2021. The copyright holder for this preprint (which was not certified by peer review) is the author/funder, who has granted bioRxiv a license to display the preprint in perpetuity. It is made available under aCC-BY-NC-ND 4.0 International license.

DISCUSSION

Modulations in micro-architectural features dominate a multitude of biological processes ranging from learning, development and plasticity to aging, neurodegeneration and neural injury. Therefore, longitudinally and noninvasively characterizing such time-dependent processes has been a desideratum for contemporary neuroimaging. Indeed, diffusion-driven methods such as DWI, DTI and DKI have played a crucial role in stroke evaluation endowed by the microscopic-scale sensitivity arising from water diffusion within cellular-scale barriers. For example, the diffusion coefficient (or tensor) based methods can detect the stroke at very early stages[45], while the DKI counterparts show larger lesion sizes[44]. However, these methods provide information that is inherently averaged along all diffusion directors, thereby reporting mesoscopic, rather than microscopic features.

Here, we developed the CTI methodology for assessing more specific microscopic features within the imaged voxels. By relying on the measurement of the 4th order displacement correlation tensor using DDE, CTI disentangles the features contributing to non-gaussian diffusion into the underlying sources: anisotropic, isotropic and microscopic variances (while still providing the more conventional metrics typically used for stroke imaging (e.g., MD, K_T, FA)). Indeed, the CTI approach dramatically improved the detection and characterization of the stroked region. In particular, (some of) its metrics provided a much more sensitive detection of the ischemic features, while the combination of its parameters provided enhanced specificity and insights into the underlying micro-architectural modulations in the tissue.

For instance, μK showed a dramatic increase and much higher sensitivity to the ischemia compared to its conventional MD and K_T counterparts. The reason for this enhanced sensitivity can be ascribed to the decoupling of the mesoscopic intravoxel orientation dependence as well as the removal of gaussian / anisotropy components, thereby leading to the μK reflecting much more of the microscopic environment. Indeed, the μK maps revealed both much stronger contrast than the conventional metrics as well as larger areas affected by

bioRxiv preprint doi: https://doi.org/10.1101/2021.02.20.432088; this version posted February 20, 2021. The copyright holder for this preprint (which was not certified by peer review) is the author/funder, who has granted bioRxiv a license to display the preprint in perpetuity. It is made available under aCC-BY-NC-ND 4.0 International license.

the stroke. Therefore, μK is a strong candidate for earlier detection of ischemia and better assessment of potential stroke severity, functional outcomes and prognosis.

From a more biological perspective, the subacute phase of ischemia investigated in this study is characterized by three major micro-architectural modulations occurring downstream of the disruption in oxygen supply. In particular (1) beading due to ongoing excitotoxicity and activated microglia; and (2) edema formation and disruption of extracellular/intracellular ionic balance; and (3) cell swelling. It is thus instructive to assess how these processes could affect the CTI metrics, at least qualitatively.

Figure 6 shows simulations for different micro-architectural scenarios. The upper panel describes the different CTI metrics for different degrees of beading. Interestingly, we find clear signatures for increased beading in CTI signals. The MD decreases (consistent with Budde et al.[16]), while total kurtosis increases, which can now be explained by strong increases in μK accompanied by small decreases in K_{aniso} (K_{iso} remains zero for all beaded scenarios by definition[38]). This, importantly, contrasts with the scenario of edema formation (c.f. Fig.6b), which shows that as the edema fraction increases (from only beads to only free water, $0 < f_{edema} < 1$), μK and K_{aniso} decrease in a similar fashion, while MD increases and total kurtosis decreases. In this case, K_{iso} first increases as the diffusivity difference between the beads and the more freely diffusing water is initially large but as the free fraction begins to dominate, the variance in diffusivities is strongly skewed to free diffusion, culminating in totally free diffusion, which has zero variance ($K_{iso} = 0$). Finally, if we consider edema formation in the presence of "swelling" of disconnected spherical objects (e.g., representing spheres, Fig. 6c), K_{aniso} remains constant and zero while K_T and K_{iso} evidence maxima in their values, and μK is negative, and increasing in value as edema fraction increases. Hence, CTI can provide unique insights into the underlying modes of micro-architectural modulations and edema formation.

Interestingly, the introduction of a more rapidly diffusing component into the system (e.g., edema) also explains the stronger WM changes observed in K_{iso}: in WM, the microstructure comprises much smaller objects (e.g., axons, myelin etc.) that are characterized by a very low diffusivity. When water with higher diffusivity is introduced to the

bioRxiv preprint doi: https://doi.org/10.1101/2021.02.20.432088; this version posted February 20, 2021. The copyright holder for this preprint (which was not certified by peer review) is the author/funder, who has granted bioRxiv a license to display the preprint in perpetuity. It is made available under aCC-BY-NC-ND 4.0 International license.

system, the isotropic variance will be strongly impacted as noted in Fig.6. By contrast, in gray matter, the initial diffusivity is higher, thereby the variance in diffusivities upon the introduction of a more rapidly diffusing moiety (e.g., edema) would be smaller than in WM, thereby also making the changes in K_{iso} lower in GM upon ischemia, consistent with our observations.

The anisotropic kurtosis source, K_{aniso} showed a large decrease both in gray matter and in white matter, with much larger decreases in GM. K_{aniso} reflects the microscopic anisotropy without the conflating effects of orientation dispersion suggesting that the spins diffuse in less anisotropic structures upon ischemia, and as shown in Figure 6, a decrease in K_{aniso} would be commensurate with increased beading.

Our findings also have several implications for dMRI modelling in health and disease. First, the often-ignored μK, clearly needs to be taken into account when modelling dMRI signals in general, as its contribution could clearly be important when looking for changes upon e.g. neurodegeneration. Ignoring μK will result in its contributions becoming conflated into the other kurtosis sources; this in turn could mislead the interpretation of the observed changes in micro-architecture. Finally, it is important to state that characterization of penumbra – which is a major goal for stroke imaging, could strongly benefit from CTI, as mismatches between the different metrics could be plotted and contrasted with, e.g., changes in perfusion. More generally, we expect that the CTI metrics will also be sensitive to other biological mechanisms underlying different diseases, aging, or changes in microstructure associated with development, learning and maturation. All these features bode well for the application of CTI in basic and applied research in the future.

bioRxiv preprint doi: https://doi.org/10.1101/2021.02.20.432088; this version posted February 20, 2021. The copyright holder for this preprint (which was not certified by peer review) is the author/funder, who has granted bioRxiv a license to display the preprint in perpetuity. It is made available under aCC-BY-NC-ND 4.0 International license.

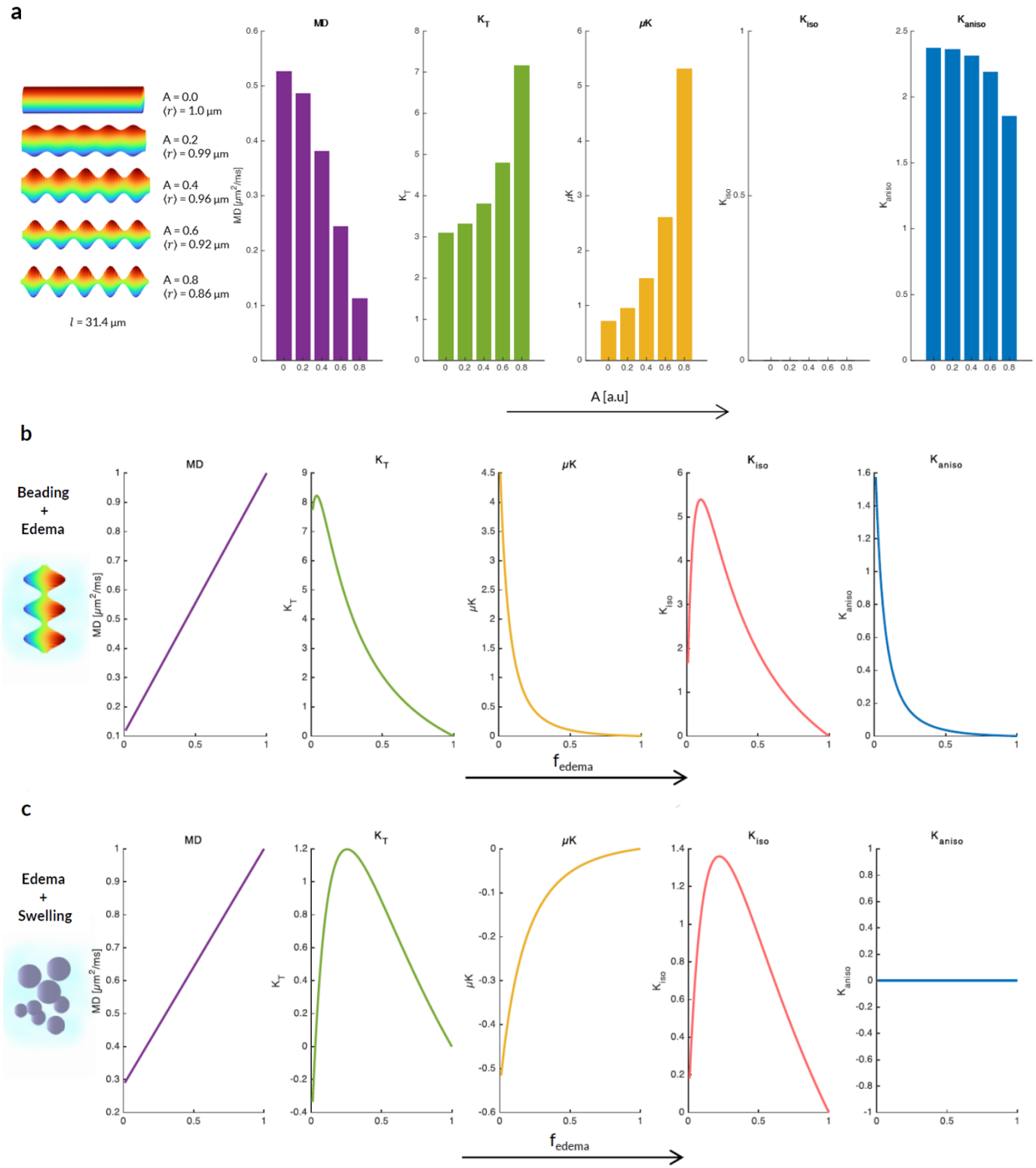

Figure 6: Kurtosis sources estimates with beading and restricted environment (beading and swelling with free water fraction) scenarios. (a) MC random walk simulations to study the effect of axon beading on the diffusion kurtosis parameters. Five simulated axons were generated by increasing A (which controls the amplitude of beading) from 0, i.e., modulation of axon without beading, to 0.8 (length = 31.4 µm). The respective conventional and novel diffusion kurtosis metrics are presented for all simulated axons scenarios (from left to right: MD [μm^2/ms], K_T, µK, K_{iso}, K_{aniso}). (b) Resulting kurtosis estimates from simulated beading effects (A = 0.8) as the free water fraction increases (modulating tissue beading as edema increases). (c) Resulting kurtosis estimates from simulated fully restricted spheres compartments with a GPD approximation size distribution (µ = 0.75 ± 0.2 µm) over a range of 100 b-values as free water fraction increases (modulating cell swelling as edema increases).

bioRxiv preprint doi: https://doi.org/10.1101/2021.02.20.432088; this version posted February 20, 2021. The copyright holder for this preprint (which was not certified by peer review) is the author/funder, who has granted bioRxiv a license to display the preprint in perpetuity. It is made available under aCC-BY-NC-ND 4.0 International license.

METHODS

Animals. Adult male C57BL/6 J mice (aged 11 weeks, weights 24-29 g, grown with a 12 h /12 h light/dark cycle with ad libitum access to food and water) were used in this study. All animal experiments were preapproved by the competent institutional and national authorities and carried out according to European Directive 2010/63.

Surgical procedures. A photothrombotic Rose Bengal stroke model[46] was used to induce a focal infarction in the barrel cortex (S1bf), previously identified upon anatomic mapping, with a solution of Rose Bengal dye (Sigma Aldrich, 95%) dissolved in sterile saline (15 mg/ml) and filtrated through a 0.2 µm sterile filter. Each mouse was injected with meloxicam (Nonsteroidal anti-inflammatory drug) 30 min prior to surgery and anesthetized with isoflurane (~ 2.5% in 28% oxygen). Temperature was monitored and maintained at 36 – 37ºC with a heating pad. The skull was exposed by a median incision of the skin at the dorsal aspect of the head and the periosteum was removed.

The solution was delivered intravenously by a retroorbital injection (10µl/g animal weight). The animals were then irradiated with a cold light source and a fiber optic light guide (0.89 mm tip) – reaching a colour temperature of 3200 K and a beam light intensity of 10 W/cm^2 – in the barrel cortex (1.67 mm posterior; 3 mm lateral to bregma[47]) for 15 minutes. A sham group (N = 5) underwent the same conditions except for the lesion-inducing illumination, yet the 15-minute interval post injection was respected.

Brain extraction and sample preparation. Brain specimens were extracted via transcardial perfusion with 4% Paraformaldehyde (PFA) from ten adult mice (N = 10) at 3 h post ischemic onset. After extraction of the skull, the brains were immersed in a 4% PFA solution for 24 h and washed in a Phosphate-Buffered Saline solution afterwards, preserved in for at least 24 h. The specimens were subsequently placed in a 10-mm NMR tube filled with Fluorinert (Sigma Aldrich, Lisbon, PT), secured with a stopper to prevent from floating. The tube was then sealed with paraffin film.

bioRxiv preprint doi: https://doi.org/10.1101/2021.02.20.432088; this version posted February 20, 2021. The copyright holder for this preprint (which was not certified by peer review) is the author/funder, who has granted bioRxiv a license to display the preprint in perpetuity. It is made available under aCC-BY-NC-ND 4.0 International license.

CTI protocol. CTI was then directly fitted to the data using a linear-least squares fitting procedure implemented to the following equation[38]:

$$\log E_{\Delta}(\boldsymbol{q}_1, \boldsymbol{q}_2) = -(q_{1i}, q_{1j} + q_{2i}, q_{2j})\Delta D_{ij} + \frac{1}{6}(q_{1i}q_{1j}q_{1k}q_{1l} + q_{2i}q_{2j}q_{2k}q_{2l})\Delta^2\overline{D}^2 W_{ijkl} + q_{1i}q_{1j}q_{2k}q_{2l}\Delta^2 C_{ijkl} + O(q^6)$$

where D_{ij}, W_{ijkl} and C_{ijkl} correspond to the diffusion, kurtosis and covariance tensors, respectively. The sources of kurtosis can be extracted from these tensors in the following way (Henriques et al., 2020): 1) the total kurtosis K_T can be computed from W_{ijkl}; 2) the two inter-compartmental kurtosis sources (K_{aniso} and K_{iso}) can be extracted from C_{ijkl}; and 3) an intra-compartmental kurtosis source K_{intra} can be estimated as $K_T - K_{aniso} - K_{iso}$.

Diffusion-imaging parameters. Imaging was performed with Paravision 6.0.1 (Bruker BioSpin MRI GmbH, Ettlingen, Germany) and TopSpin 3.1. All ex vivo MRI scans were performed on a 16.4 T Aeon Ascend Bruker scanner (Karlsruhe, Germany) equipped with an AVANCE IIIHD console and a Micro5 probe with gradient coils capable of producing up to 3000 mT/m in all directions and a birdcage RF volume coil. Once inserted, the samples were maintained at 37ºC due to the probe's variable temperature capability and were allowed to acclimatize with the surroundings for at least 2 h prior to the beginning of diffusion MRI experiments. In favour of shimming, a B_0 map was also acquired covering the volume of the brain.

Double diffusion encoding data were subsequently acquired for 25 coronal slices using an in house written EPI-based DDE pulse sequence. The diffusion encoding gradient pulse separation Δ and mixing time τ_m were set to 10 ms, and the pulsed gradient duration δ was set to 1.5 ms. Acquisitions were repeated for five q_1-q_2 magnitude combinations (1498 - 0, 1059.2 - 1059.2, 1059.2 - 0, 749.0 - 749.0 and 749.0 - 0 mT/m) in which equal magnitude q_1-q_2 combinations were repeated for 135 parallel and perpendicular directions, reflecting the

bioRxiv preprint doi: https://doi.org/10.1101/2021.02.20.432088; this version posted February 20, 2021. The copyright holder for this preprint (which was not certified by peer review) is the author/funder, who has granted bioRxiv a license to display the preprint in perpetuity. It is made available under aCC-BY-NC-ND 4.0 International license.

necessary diffusion gradient intensities for the requirements of the CTI protocol to be fulfilled (for the tensors associated with the fourth cumulant to be fitted). In this study, the selected gradient intensities were 3000, 1500 or 750 mm/s^2. In addition, twenty acquisitions without any diffusion-weighted sensitization (zero b-value) were performed to guarantee a high ratio between the number of non-diffusion and diffusion-weighted acquisitions. For all experiments, the following parameters were used: TR/TE = 3000/49 ms, Field of View = 11 × 11 mm^2, matrix size 78 × 78, resulting in an in-plane voxel resolution of 141 × 141 µm^2, slice thickness = 0.5 mm, number of segments = 2, number of averages = 8. For every b_{max} value, the total acquisition time was approximately 1 h and 57 min.

Structural MRI parameters. Axial and sagittal T2-weighted images with high resolution and high SNR were acquired for anatomical reference. These data were acquired using RARE pulse sequences with the following parameters: TR = 4000 ms, TE = 50 ms, RARE factor = 12, number of averages = 6. Concerning the axial images, the Field of View (FOV) was 18 × 18 mm^2, and the matrix size was 240 × 132, resulting in an in-plane voxel resolution of 75 × 76 µm^2. For the sagittal images, FOV was set to 18 × 9 mm^2, matrix size to 240 × 120, and subsequently in-plane voxel resolution resulted in 75 × 75 µm^2 (sagittal). Both axial and sagittal acquisitions sampled the total of 33 slices with a thickness of 0.3 mm. For the coronal images, FOV was established as 10.5 × 10.5 mm^2, the matrix size as 140 × 140, hence an in-plane voxel resolution of 75 × 75 µm2 , for 72 slices 0.225 mm thick. The MRI infarct volumes were calculated by the amount of voxels within the designated masks multiplied by the volume of each voxel.

Diffusion data pre-processing. Before starting the diffusion data analysis, masks for all slice delineation were manually drawn on Matlab (Matlab R2018b). All datasets were corrected for Gibbs ringing artifacts[48,49] in Python (Dipy, version 1.0[50]) which suppresses the Gibbs oscillations effects based on a total local variation (TV) analysis. In this case, TV was accessed with three neighbours and hence the artefact correction was done based on three adjacent points for each voxel. All diffusion-weighted datasets underwent realignment via a

bioRxiv preprint doi: https://doi.org/10.1101/2021.02.20.432088; this version posted February 20, 2021. The copyright holder for this preprint (which was not certified by peer review) is the author/funder, who has granted bioRxiv a license to display the preprint in perpetuity. It is made available under aCC-BY-NC-ND 4.0 International license.

sub-pixel registration method[51] in which each set of data for every total diffusion b-value would be realigned to a counter defined dataset with similar DDE gradient pattern combinations.

Diffusion data post-processing. CTI was then directly fitted to the data (normalized to b0 images – images without diffusion gradient weighting) using linear least squares, implemented in-house. The parameters were estimated by fitting CTI to data using all the acquired b-values.

Region of Interest Analysis. (Specificity assessment) A region of Interest (ROI) analysis was performed by manual selection of the most relevant areas for every diffusion data slice in both hemispheres in all brains, containing the total lesion and counterpart region in the opposite hemisphere, and subsequent threshold selection of gray and white matter within the manually selected ROIs. For each brain sample which had previously undergone ischemic insult and considering the previously selected ROI covering the total lesion area in the MD measure map, an identically sized ROI (and symmetrical in location to the former) was manually drawn. Identical regions were then delineated on the sham group hemispheres. Within these primarily drawn ROIs, GM and WM regions were selected according to threshold values pre-established for FA and MD measures. (Sensitivity assessment) To assess which metrics were more sensitive to stroke, total ROIs were also manually drawn for each considered metric according to interhemispheric visual asymmetry. White matter ROIs were manually drawn within the total ROI according to FA maps. All ROI analyses were performed in Matlab (Matlab R2018b) (Fig.S6-7).

Statistical analysis features. A statistical specificity analysis was conducted to assess whether the differences between mean values in each ROI for each metric averaged across mice (from each group) were significant through a one-way ANOVA test, and a Bonferroni correction was performed for multiple comparisons across the different diffusion metrics. For the sensitivity analysis, a one-way ANOVA test with a subsequent Bonferroni correction were also performed to test if the differences in interhemispheric ratio percentage changes between ipsilesional-contralesional (stroked brain) and ipsilesional (stroked brain) and ipsilateral (control brain) were significant. A similar analysis was performed to assess

bioRxiv preprint doi: https://doi.org/10.1101/2021.02.20.432088; this version posted February 20, 2021. The copyright holder for this preprint (which was not certified by peer review) is the author/funder, who has granted bioRxiv a license to display the preprint in perpetuity. It is made available under aCC-BY-NC-ND 4.0 International license.

significant differences between the number of voxels which, based on manually drawn ROIs, were abnormal when compared with the contralesional hemisphere of the stroked group and for all kurtosis sources. All statistical analysis were performed in Matlab (Matlab R2018b).

Data visualization. All volumetric datasets were rendered with ImageJ. Volume render maps were produced using tricubic smooth interpolation for KT and µK sources.

Simulations. Monte Carlo random walk simulations were performed to study the effect of axon beading on the diffusion kurtosis parameters. An axon without beading was modelled as an impermeable cylinder (length = 31.4 µm, radius = 1 µm) aligned with the z-axis. Beading was introduced by making the radius depend on the location along the z-axis: $r(z) = r_0 + A \cdot \sin(B \cdot z)$, where r_0 is the mean radius, $A \in [0,1]$ controls the amplitude of beading, and B controls the frequency and location of beading. Five simulated axons, shown in Figure X, were generated by increasing A from 0 to 0.8 in equal steps and adjusting r_0 to keep the volume constant. B = 1 μm^{-1} for all simulated axons (Fig.6a).

Simulated data was generated using Disimpy[52] with 10^5 random walkers, 10^4 time steps, and diffusivity of 2 μm^2/ms. The initial positions of the random walkers were randomly sampled from a uniform distribution inside the axons. MR signals were generated using pulsed gradient single diffusion encoding with δ = 1.5 ms and Δ = 10 ms, 60 diffusion encoding directions uniformly distributed over the surface of half a sphere, and 10 b-values uniformly distributed between 0 and 3 ms/μm^2. The diffusion and kurtosis tensors were estimated from the simulated signals using a weighted linear least squares fit in Dipy[50]. MD, µK, K_{iso}, and K_{aniso} were calculated from the diffusion tensor eigenvalues and the elements of the kurtosis tensor[38] (Fig.6a).

Analytically computed pulsed gradient spin echo sequence signals were simulated for two different models using the MISST toolbox[53–56]: beading (to model beaded axons) with formation of edema, assuming the most beaded previously simulated scenario with A = 0.8 (Fig.6b); spherical compartments with restricted diffusion (to model cell swelling) and

bioRxiv preprint doi: https://doi.org/10.1101/2021.02.20.432088; this version posted February 20, 2021. The copyright holder for this preprint (which was not certified by peer review) is the author/funder, who has granted bioRxiv a license to display the preprint in perpetuity. It is made available under aCC-BY-NC-ND 4.0 International license.

formation of edema, with combinations of radii between 0.8×10^{-6} m and 10×10^{-6} m, with a diffusivity value of 2×10^{-9} m/s^2 (Fig.6c).

Nissl Cresyl Violet staining. Histological analysis was performed in one of the stroked ex vivo samples. Slices were obtained through Vibratome sectioning with a thickness of 0.04 mm and Mowiol containing 2.5 % 1,4 diazobicyclo-[2.2.2]-octane (DABCO, Sigma, D2522) was used as the mounting media. The brain sections were then fixed with 10% formalin and processed with Nissl-Cresyl Violet staining for microscopy in order to assess tissue damage and cell loss within the infarcted region.

Optical imaging. Histological imaging was performed with a ZEISS Axio Scan.Z1 (Zeiss, Germany) coupled to a Hitachi 3 CCD colour camera and processed with QuPath 0.2.3 (Fig.2e). Images were magnified (53×) for both ipsi- and contralesional hemispheres.

Animal monitoring for in vivo MRI imaging. For anaesthesia induction, the body temperature of the mouse was kept constant by placing the animal on top of an electrical heating pad. Anaesthesia with a mixture of medical air and 4% isoflurane (Vetflurane, Virbac, France) was maintained until the animal righting reflex and any reaction to firm foot squeeze were lost. The isoflurane concentration was regulated and reduced to 2.5%. The mouse was then weighed and transferred to the animal bed, prone positioned above a heated water pad – in order for the mouse body temperature not to oscillate during the experiments –, having its head placed with its upper incisors held on to a mouth bite bar. Oxygen concentrations were kept between 27% and 28%, monitored by a portable oxygen monitor (MX300-I, Viamed, United Kingdom). Ear bars were used for a safe and efficient head fixation (into external meatus) and eye ointment (Bepanthen Eye Drops, Bepanthen, Germany) was applied to prevent the corneas from drying. A rectal temperature probe and a respiration sensor (Model 1030 Monitoring Gating System, SAII, United States of America) were placed for real-time monitoring of these physiological measurements to guarantee the animal's welfare and immobilization. Considering the water molecules sensitivity towards temperature alterations, the waterbed temperature was cautiously monitored and controlled to avoid oscillations.

bioRxiv preprint doi: https://doi.org/10.1101/2021.02.20.432088; this version posted February 20, 2021. The copyright holder for this preprint (which was not certified by peer review) is the author/funder, who has granted bioRxiv a license to display the preprint in perpetuity. It is made available under aCC-BY-NC-ND 4.0 International license.

Respiration rates were also monitored and maintained at physiological levels throughout dMRI scanning.

Diffusion-imaging parameters in vivo. Imaging was executed with Paravision 6.0.1 (Bruker BioSpin MRI GmbH, Ettlingen, Germany) and TopSpin 3.1. The in vivo MRI data were acquired on a 9.4 T horizontal MRI scanner (BioSpec 94/20 USR, Bruker BioSpin, Germany) equipped a gradient system able to produce up to 660 mT/m in every direction, an 86 mm quadrature coil for transmission and a 4-element array surface cryocoil for reception.

Sagittal T2-weighted images were acquired for anatomical reference using a RARE pulse sequence with the following parameters: TR = 2000 ms, TE = 36 ms, RARE factor = 8, number of averages = 8. The field of view was 24 × 16.1 mm^2, the matrix size was 256 × 256 , resulting in an in-plane voxel resolution of 150 × 150 μm^2. The slice thickness was 0.5 mm, and 21 slices were sampled.

Following an optimized protocol when compared to the ex vivo experiment, DDE data were acquired for 5 coronal slices using an in house written EPI-based DDE pulse sequence. The diffusion encoding gradient pulse separation Δ and mixing time τ_m were set to 10 ms, and the pulsed gradient duration δ was set to 4 ms. Acquisitions were repeated for five q_1-q_2 magnitude combinations (518.79 - 0, 366.84 – 366.84.2, 366.84 - 0, 259.4 – 259.4 and 259.4 - 0 mT/m), following equal combinations of directions as in the ex vivo experiments (Figure 3.10). In addition, twenty acquisitions without any diffusion-weighted sensitization (b-value = 0) were performed. For all experiments, the following parameters were used: TR/TE = 2800/44.5 ms, FOV = 12 × 12 mm^2, matrix size 78 × 78, resulting in an in-plane voxel resolution of 181 × 181 μm^2, slice thickness = 0.85 mm, number of segments = 1, number of averages = 1 and partial Fourier acceleration of 1.25. For every b_{max} value, the total acquisition time was approximately 7 min.

Data availability. The data sets generated and analysed during the current study are available from the corresponding author upon reasonable request.

bioRxiv preprint doi: https://doi.org/10.1101/2021.02.20.432088; this version posted February 20, 2021. The copyright holder for this preprint (which was not certified by peer review) is the author/funder, who has granted bioRxiv a license to display the preprint in perpetuity. It is made available under aCC-BY-NC-ND 4.0 International license.

Code availability. Custom MATLAB code for dMRI pre- and post-processing of data is available from the corresponding author upon reasonable request.

ACKNOWLEDGMENTS

This study was funded by the European Research Council (ERC) under the European Union's Horizon 2020 research and innovation programme (Starting Grant, agreement No. 679058). The authors acknowledge the vivarium of the Champalimaud Centre for the Unknow, a facility of CONGENTO financed by Lisboa Regional Operational Programme (Lisboa 2020), project LISBOA01-0145-FEDER-022170, and also the Champalimaud Histopathology and the Champalimaud ABBE Platforms. The authors also want to thank Ms. Beatriz Cardoso for assistance in the preparation of the ex vivo mouse brain specimens.

bioRxiv preprint doi: https://doi.org/10.1101/2021.02.20.432088; this version posted February 20, 2021. The copyright holder for this preprint (which was not certified by peer review) is the author/funder, who has granted bioRxiv a license to display the preprint in perpetuity. It is made available under aCC-BY-NC-ND 4.0 International license.

REFERENCES

1. Suter, T. A. C. S. & Jaworski, A. Cell migration and axon guidance at the border between central and peripheral nervous system. Science 365, (2019).
2. Hughes, E. G., Orthmann-Murphy, J. L., Langseth, A. J. & Bergles, D. E. Myelin remodeling through experience-dependent oligodendrogenesis in the adult somatosensory cortex. Nat. Neurosci. 21, 696–706 (2018).
3. Brodt, S. et al. Fast track to the neocortex: A memory engram in the posterior parietal cortex. Science 362, 1045–1048 (2018).
4. Zatorre, R. J., Fields, R. D. & Johansen-Berg, H. Plasticity in gray and white: neuroimaging changes in brain structure during learning. Nat. Neurosci. 15, 528–536 (2012).
5. Scholz, J., Klein, M. C., Behrens, T. E. J. & Johansen-Berg, H. Training induces changes in white-matter architecture. Nat. Neurosci. 12, 1370–1371 (2009).
6. Craddock, R. C. et al. Imaging human connectomes at the macroscale. Nat. Methods 10, 524–539 (2013).
7. Pestilli, F., Yeatman, J. D., Rokem, A., Kay, K. N. & Wandell, B. A. Evaluation and statistical inference for human connectomes. Nat. Methods 11, 1058–1063 (2014).
8. Hill, R. A., Li, A. M. & Grutzendler, J. Lifelong cortical myelin plasticity and age-related degeneration in the live mammalian brain. Nat. Neurosci. 21, 683–695 (2018).
9. Murphy, T. H. & Corbett, D. Plasticity during stroke recovery: From synapse to behaviour. Nat. Rev. Neurosci. 10, 861–872 (2009).
10. Li, N. et al. mTOR-Dependent Synapse Formation Underlies the Rapid Antidepressant Effects of NMDA Antagonists. Science 329, 959–964 (2010).
11. Peelaerts, W. et al. α-Synuclein strains cause distinct synucleinopathies after local and systemic administration. Nature 522, 340–344 (2015).
12. De Strooper, B. & Karran, E. The Cellular Phase of Alzheimer's Disease. Cell 164, 603–

bioRxiv preprint doi: https://doi.org/10.1101/2021.02.20.432088; this version posted February 20, 2021. The copyright holder for this preprint (which was not certified by peer review) is the author/funder, who has granted bioRxiv a license to display the preprint in perpetuity. It is made available under aCC-BY-NC-ND 4.0 International license.

615 (2016).

13. Budde, M. D., Janes, L., Gold, E., Turtzo, L. C. & Frank, J. A. The contribution of gliosis to diffusion tensor anisotropy and tractography following traumatic brain injury: validation in the rat using Fourier analysis of stained tissue sections. Brain 134, 2248–2260 (2011).

14. Mathers, C. et al. WHO methods and data sources for country- level causes of death 2000- 2015.(2017). Available at: https://www.who.int/healthinfo/global_burden_disease/GlobalCOD_method_2000_2015.pdf?ua=1.

15. Xing, C., Arai, K., Lo, E. H. & Hommel, M. Pathophysiologic cascades in ischemic stroke. Int. J. Stroke 7, 378–385 (2012).

16. Budde, M. D. & Frank, J. A. Neurite beading is sufficient to decrease the apparent diffusion coefficient after ischemic stroke. Proc. Natl. Acad. Sci. U. S. A. 107, 14472–14477 (2010).

17. Zeiler, S. R. et al. Paradoxical Motor Recovery From a First Stroke After Induction of a Second Stroke. Neurorehabil. Neural Repair 30, 794–800 (2016).

18. Veraart, J. et al. Noninvasive quantification of axon radii using diffusion MRI. Elife 9, (2020).

19. Andersson, M. et al. Axon morphology is modulated by the local environment and impacts the noninvasive investigation of its structure–function relationship. Proc. Natl. Acad. Sci. 117, 33649–33659 (2020).

20. Le Bihan, D. Looking into the functional architecture of the brain with diffusion MRI. Nat. Rev. Neurosci. 4, 469–480 (2003).

21. Novikov, D. S., Jensen, J. H., Helpern, J. A. & Fieremans, E. Revealing mesoscopic structural universality with diffusion. Proc. Natl. Acad. Sci. 111, 5088–5093 (2014).

22. Moseley, M. E. et al. Early detection of regional cerebral ischemia in cats: Comparison of diffusion- and T2- weighted MRI and spectroscopy. Magn. Reson. Med. 14, 330–

bioRxiv preprint doi: https://doi.org/10.1101/2021.02.20.432088; this version posted February 20, 2021. The copyright holder for this preprint (which was not certified by peer review) is the author/funder, who has granted bioRxiv a license to display the preprint in perpetuity. It is made available under aCC-BY-NC-ND 4.0 International license.

346 (1990).

23. Karbasforoushan, H., Cohen-Adad, J. & Dewald, J. P. A. Brainstem and spinal cord MRI identifies altered sensorimotor pathways post-stroke. Nat. Commun. 10, 3524 (2019).

24. Clark, W. M. et al. Recombinant Tissue-Type Plasminogen Activator (Alteplase) for Ischemic Stroke 3 to 5 Hours After Symptom Onset. JAMA 282, 2019 (1999).

25. Basser, P. J., Mattiello, J. & LeBihan, D. MR diffusion tensor spectroscopy and imaging. Biophys. J. 66, 259–267 (1994).

26. Jensen, J. H., Helpern, J. A., Ramani, A., Lu, H. & Kaczynski, K. Diffusional kurtosis imaging: The quantification of non-gaussian water diffusion by means of magnetic resonance imaging. Magn. Reson. Med. 53, 1432–1440 (2005).

27. Stejskal, E. O. & Tanner, J. E. Spin diffusion measurements: Spin echoes in the presence of a time-dependent field gradient. J. Chem. Phys. 42, 288–292 (1965).

28. Shemesh, N. et al. Conventions and Nomenclature for Double Diffusion Encoding NMR and MRI. Magn. Reson. Med. 87, 82–87 (2016).

29. Lee, H. H., Papaioannou, A., Kim, S. L., Novikov, D. S. & Fieremans, E. A time-dependent diffusion MRI signature of axon caliber variations and beading. Commun. Biol. 3, (2020).

30. Moseley, M. E. et al. Diffusion-weighted MR imaging of acute stroke: Correlation with T2-weighted and magnetic susceptibility-enhanced MR imaging in cats. Am. J. Neuroradiol. 11, 423–429 (1990).

31. Baron, C. A. et al. Reduction of Diffusion-Weighted Imaging Contrast of Acute Ischemic Stroke at Short Diffusion Times. Stroke 46, 2136–2141 (2015).

32. Novikov, D. S., Fieremans, E., Jespersen, S. N. & Kiselev, V. G. Quantifying brain microstructure with diffusion MRI: Theory and parameter estimation. NMR Biomed. 32, e3998 (2019).

bioRxiv preprint doi: https://doi.org/10.1101/2021.02.20.432088; this version posted February 20, 2021. The copyright holder for this preprint (which was not certified by peer review) is the author/funder, who has granted bioRxiv a license to display the preprint in perpetuity. It is made available under aCC-BY-NC-ND 4.0 International license.

33. Szafer, A., Zhong, J. & Gore, J. C. Theoretical Model for Water Diffusion in Tissues. Magn. Reson. Med. 33, 697–712 (1995).

34. Weber, R. A. et al. Diffusional kurtosis and diffusion tensor imaging reveal different time-sensitive stroke-induced microstructural changes. Stroke 46, 545–550 (2015).

35. Mitra, P. P. Multiple wave-vector extensions of the NMR pulsed-field-gradient spin-echo diffusion measurement. Phys. Rev. 51, 74–78 (1995).

36. Jespersen, S. N., Lundell, H., Sønderby, C. K. & Dyrby, T. B. Orientationally invariant metrics of apparent compartment eccentricity from double pulsed field gradient diffusion experiments. NMR Biomed. 26, 1647–1662 (2013).

37. Nørhøj, S. & Buhl, N. The displacement correlation tensor : Microstructure , ensemble anisotropy and curving fibers. J. Magn. Reson. Imaging 208, 34–43 (2011).

38. Henriques, R. N., Jespersen, S. N. & Shemesh, N. Correlation tensor magnetic resonance imaging. Neuroimage 211, (2020).

39. Kerkelä, L., Henriques, R. N., Hall, M. G., Clark, C. A. & Shemesh, N. Validation and noise robustness assessment of microscopic anisotropy estimation with clinically feasible double diffusion encoding MRI. Magn. Reson. Med. 1–13 (2019).

40. Nilsson, M. et al. Tensor- valued diffusion MRI in under 3 minutes: an initial survey of microscopic anisotropy and tissue heterogeneity in intracranial tumors. Magn. Reson. Med. 83, 608–620 (2020).

41. Callaghan, P. T. Pulsed-Gradient Spin-Echo NMR for Planar, Cylindrical, and Spherical Pores under Conditions of Wall Relaxation. J. Magn. Reson. Ser. A 113, 53–59 (1995).

42. Callaghan, P. T., Coy, A., MacGowan, D., Packer, K. J. & Zelaya, F. O. Diffraction-like effects in NMR diffusion studies of fluids in porous solids. Nature 351, 467–469 (1991).

43. Hui, E. S. et al. Stroke assessment with diffusional kurtosis imaging. Stroke 43, 2968–2973 (2012).

44. Umesh Rudrapatna, S. et al. Can diffusion kurtosis imaging improve the sensitivity and specificity of detecting microstructural alterations in brain tissue chronically after

bioRxiv preprint doi: https://doi.org/10.1101/2021.02.20.432088; this version posted February 20, 2021. The copyright holder for this preprint (which was not certified by peer review) is the author/funder, who has granted bioRxiv a license to display the preprint in perpetuity. It is made available under aCC-BY-NC-ND 4.0 International license.

experimental stroke? Comparisons with diffusion tensor imaging and histology. Neuroimage 97, 363–373 (2014).

45. Sotak, C. H. The role of diffusion tensor imaging in the evaluation of ischemic brain - A review. NMR Biomed. 15, 561–569 (2002).

46. Watson, B. D., Dietrich, W. D., Busto, R., Wachtel, M. S. & Ginsberg, M. D. Induction of reproducible brain infarction by photochemically initiated thrombosis. Ann. Neurol. 17, 497–504 (1985).

47. Franklin, K. & Paxinos, G. *Paxinos and Franklin's the Mouse Brain in Stereotaxic* Coordinates. (2019).

48. Henriques, R. N. Advanced Methods for Diffusion MRI Data Analysis and their Application to the Healthy Ageing Brain. (Cambridge University, 2018). doi:10.17863/CAM.29356

49. Kellner, E., Dhital, B., Kiselev, V. G. & Reisert, M. Gibbs-ringing artifact removal based on local subvoxel-shifts. Magn. Reson. Med. 76, 1574–1581 (2016).

50. Garyfallidis, E. et al. Dipy, a library for the analysis of diffusion MRI data. Front. Neuroinform. 8, (2014).

51. Guizar-sicairos, M., Thurman, S. T. & Fienup, J. R. Guizar_Efficent_subpixel_. Opt. Lett. 33, 156–158 (2008).

52. Kerkelä, L., Nery, F., Hall, M. & Clark, C. Disimpy: A massively parallel Monte Carlo simulator for generating diffusion-weighted MRI data in Python. J. Open Source Softw. 5, 2527 (2020).

53. Drobnjak, I., Siow, B. & Alexander, D. C. Optimizing gradient waveforms for microstructure sensitivity in diffusion-weighted MR. J. Magn. Reson. 206, 41–51 (2010).

54. Drobnjak, I., Zhang, H., Hall, M. G. & Alexander, D. C. The matrix formalism for generalised gradients with time-varying orientation in diffusion NMR. J. Magn. Reson. 210, 151–157 (2011).

55. Ianuş, A., Siow, B., Drobnjak, I., Zhang, H. & Alexander, D. C. Gaussian phase distribution approximations for oscillating gradient spin echo diffusion MRI. J. Magn.

bioRxiv preprint doi: https://doi.org/10.1101/2021.02.20.432088; this version posted February 20, 2021. The copyright holder for this preprint (which was not certified by peer review) is the author/funder, who has granted bioRxiv a license to display the preprint in perpetuity. It is made available under aCC-BY-NC-ND 4.0 International license.

Reson. 227, 25–34 (2013).

56. Ianuş, A., Alexander, D. C. & Drobnjak, I. Microstructure Imaging Sequence Simulation Toolbox. in 34–44 (2016). doi:10.1007/978-3-319-46630-9_4